JOURNAL OF GEOPHYSICAL RESEARCH, VOL. 115, A02303, doi:10.1029/2009JA014697, 2010

First *E* region observations of mesoscale neutral wind interaction with auroral arcs

M. J. Kosch,[1] C. Anderson,[2] R. A. Makarevich,[2] B. A. Carter,[2] R. A. D. Fiori,[3,4] M. Conde,[5] P. L. Dyson,[2] and T. Davies[2]

Received 28 July 2009; revised 5 October 2009; accepted 7 October 2009; published 3 February 2010.

[1] We report the first observations of *E* region neutral wind fields and their interaction with auroral arcs at mesoscale spatial resolution during geomagnetically quiet conditions at Mawson, Antarctica. This was achieved by using a scanning Doppler imager, which can observe thermospheric neutral line-of-sight winds and temperatures simultaneously over a wide field of view. In two cases, the background *E* region wind field was perpendicular to an auroral arc, which when it appeared caused the wind direction within ~50 km of the arc to rotate parallel along the arc, reverting to the background flow direction when the arc disappeared. This was observed under both westward and eastward plasma convection. The wind rotations occurred within 7–16 min. In one case, as an auroral arc propagated from the horizon toward the local zenith, the background *E* region wind field became significantly weaker but remained unaffected where the arc had not passed through. We demonstrate through modeling that these effects cannot be explained by height changes in the emission layer. The most likely explanation seems to be the greatly enhanced ion drag associated with the increased plasma density and localized ionospheric electric field associated with auroral arcs. In all cases, the *F* region neutral wind appeared less affected by the auroral arc, although its presence is clear in the data.

Citation: Kosch, M. J., C. Anderson, R. A. Makarevich, B. A. Carter, R. A. D. Fiori, M. Conde, P. L. Dyson, and T. Davies (2010), First *E* region observations of mesoscale neutral wind interaction with auroral arcs, *J. Geophys. Res.*, *115*, A02303, doi:10.1029/2009JA014697.

1. Introduction

[2] At high latitudes, magnetosphere-ionosphere coupling is achieved through large-scale field-aligned current (FAC) systems [e.g., *Iijima and Potemra*, 1976; *Kosch and Nielsen*, 2001; *Zmuda and Armstrong*, 1974]. In the premagnetic midnight dusk sector, downward FACs flow equatorward of the upward return currents and vice versa in the postmagnetic midnight dawn sector. The large-scale morphology of the FACs is controlled by the B_z and B_y components of the interplanetary magnetic field (IMF) [*Weimer*, 2001]. For B_z negative, the statistical strength of the FAC is controlled by the amplitude of B_z [*Kosch and Nielsen*, 2001]. For B_z positive, the FAC strength weakens and breaks up into multiple zones [*Friis-Christensen et al.*, 1985; *Iijima and Shibaji*, 1987]. These currents close via poleward (equatorward) ionospheric Pedersen currents in the dusk (dawn) sector and dissipate energy via Joule heating, expressed by

$$Q_{\mathrm{JH}} = E^2 \Sigma_P, \tag{1}$$

where E is the electric field magnitude and Σ_P is the height-integrated Pedersen conductance [*Kosch and Nielsen*, 1995]. Joule heating is largely an *E* region phenomenon in the ionosphere [*Brekke and Rino*, 1978].

[3] The Earth's upper atmosphere between 100 and 300 km altitude consists mostly of neutral oxygen atoms and nitrogen molecules, of which <1% is ionized. The large-scale pattern of high-latitude ionospheric circulation is primarily driven by the solar wind through magnetic reconnection of the IMF with the Earth's geomagnetic field [e.g., *Chisham et al.*, 2007]. This large-scale circulation results in antisunward flow over the polar cap and westward (eastward) plasma flow in the high-latitude dusk (dawn) ionosphere. The plasma velocity is given by

$$\mathbf{v} = \frac{\mathbf{E} \times \mathbf{B}}{B^2}, \tag{2}$$

where **E** is the ionospheric electric field imposed by the magnetosphere and **B** is the Earth's magnetic field. Hence,

[1]Department of Communication Systems, Lancaster University, Lancaster, UK.
[2]Department of Physics, La Trobe University, Melbourne, Victoria, Australia.
[3]ISAS, University of Saskatchewan, Saskatoon, Saskatchewan, Canada.
[4]Also at Geomagnetic Laboratory, Natural Resources Canada, Ottawa, Ontario, Canada.
[5]Geophysical Institute, University of Alaska Fairbanks, Fairbanks, Alaska, USA.

0148-0227/10/2009JA014697$09.00

in the near-collisionless F layer, the high-latitude ionospheric electric field is poleward (equatorward) in the dusk (dawn) sector. The shape and size of the large-scale plasma convection cells depend largely on the value of the IMF B_z and B_y components. For B_z negative, a single circulation cell exists in each of the dawn and dusk sectors, and the plasma flow speed is largely a function of the magnitude of B_z. The relative size and shape of the cells is regulated by B_y. For B_y negative, the dawn cell is larger and vice versa. If B_z is significantly positive, then more than two circulation cells can develop, consisting of weak plasma flow [*Friis-Christensen et al.*, 1985; *Chisham et al.*, 2007].

[4] It is well established that high-latitude thermospheric neutral circulation is driven by ion drag, solar-heating pressure, advection (momentum), and viscous and Coriolis forces. Ion drag through ion-neutral collisions and pressure gradients due to solar heating are normally the dominant driving forces in the F layer [e.g., *Killeen and Roble*, 1984], but advection, solar heating, and Coriolis forces may all exceed the ion drag force, depending on the plasma density height profile [*Crickmore*, 1995]. Just as large-scale plasma convection is strongly influenced by B_z and B_y polarity, so too is the upper thermospheric large-scale neutral circulation [e.g., *Thayer et al.*, 1987]. Solar heating and Coriolis are normally the dominant driving forces in the E layer, although ion drag and advection may be important, depending again on the plasma density [e.g., *Killeen and Roble*, 1984, 1986]. At high latitudes, auroral precipitation frequently enhances the E region plasma density by an order of magnitude or more. E region winds maximize around 100–110 km altitude, with maximum speeds exceeding 100 m/s, and may experience a large shear with a vertical scale of 10 km or less [*Larsen*, 2002]. Following *Nozawa and Brekke* [1995], and ignoring all forces except ion drag, the neutral wind acceleration is given by

$$\frac{\partial \mathbf{u}}{\partial t} = -\nu_{in}(\mathbf{u} - \mathbf{v}), \tag{3}$$

where $\mathbf{u}$ and $\mathbf{v}$ are the neutral and plasma flow vectors, respectively, and ν_{in} is the ion-neutral collision frequency. From this simplified equation, it is obvious that ion drag is essentially a function of the ion-neutral collision frequency, which is primarily a function of neutral density in the thermosphere [*Schunk and Walker*, 1973]. Thermospheric F layer circulation broadly follows plasma convection with an e-folding time of 0.5–3.5 h [*Heelis et al.*, 2002; *Killeen and Roble*, 1984, 1988; *Kosch et al.*, 2001a], depending on geomagnetic activity. The e-folding time is given by

$$\tau_{in} = \frac{n_n}{n_i}\frac{1}{\nu_{in}} \quad \text{s}, \tag{4}$$

where n_n and n_i are the neutral and ion density, respectively. The ion drag e-folding time has not been measured in the E layer. However, since the ion-neutral collision frequency is linear with neutral density, the change in e-folding time essentially becomes a function of plasma density with altitude [*Schunk and Walker*, 1973]. Therefore, the e-folding time in the E layer may be more than an order of magnitude greater compared with the F layer but will be highly variable at high latitudes, decreasing during auroral precipitation. The strength of the FAC, ionospheric Joule heating, plasma convection, and neutral winds are all increased during geomagnetic activity and auroral substorms but never disappear completely even during quiet periods [e.g., *Aruliah et al.*, 1991; *Kosch and Nielsen*, 1995, 2001; *McCormac et al.*, 1987; *Senior et al.*, 1990].

[5] The spatial scales of the ionospheric auroral plasma can vary from the whole auroral oval down to the Debye length limit [*Galperin*, 2001]. In particular, auroral arcs may be hundreds to even thousands of kilometers geomagnetic east-west aligned, but the average optical width of steady state auroral arcs is only 18 ± 9 km [*Knudsen et al.*, 2001]. Auroral precipitation is associated with FACs and local changes in ionospheric conductivity [e.g., *Kosch et al.*, 2001b]. The FACs close through the ionosphere, dissipating energy in the form of Joule heating (see equation (1)), which is a function of the local electric field and Pedersen conductance [e.g., *Kosch and Nielsen*, 1995]. *Codrescu et al.* [2000] have shown that small-scale electric field variability leads to the situation in which the average and variable components have equal contributions to the total ionospheric Joule heating. In addition, using a single azimuth scanning Fabry-Perot interferometer (FPI) with tristatic radar plasma flow observations, *Cierpka et al.* [2000] showed that ignoring the neutral wind when estimating the ionospheric electric field resulted in an error of up to 60% in the Joule-heating calculation, at least in the F layer. Using tristatic observations of the F layer plasma and neutral flow vectors at a single point, *Aruliah et al.* [2004] found that the neutral wind dynamo was on average 50% of the magnetospheric electric field and contributes an average 41% of in situ Joule heating. A similar study has not been done in the E layer, although *Brekke and Rino* [1978] found that the maximum in ionospheric Joule heating occurred around 110–130 km altitude. Hence, it is clear that mesoscale observations of the ionospheric electric field and Pedersen conductance as well as the thermospheric neutral winds in the E layer are important. In the past, such spatial resolution has not normally been available, especially for the neutral winds, over a wide field of view.

[6] Despite the conventional wisdom that the neutral thermosphere forms a quasi steady state background to the ionosphere, there is increasing evidence that mesoscale variability in the thermospheric winds is a common feature. For example, E region vertical winds of several tens of m/s over periods of a few tens of minutes and F region vertical winds exceeding 100 m/s for periods of several hours [e.g., *Price and Jacka*, 1991; *Price et al.*, 1995; *Rees et al.*, 1984a, 1984b] may result from ionospheric Joule heating during auroral activity. *Price et al.* [1995] estimated the horizontal extent of the vertical motion was <800 km and <320 km in the F and E regions, respectively. However, *Kosch et al.* [2000b] found that both E and F region vertical winds, measured 50 km apart in the auroral zone, were essentially uncorrelated. Using a chain of three azimuth scanning FPIs, *Aruliah and Griffin* [2001] provided evidence of mesoscale thermospheric variability in the horizontal winds. Subsequently, using tristatic observations of the F layer plasma and neutral flow vectors at a single point, *Aruliah et al.* [2005] found that the F layer thermosphere was significantly variable on a time scale of minutes and a spatial scale of a

few hundred kilometers. Increasing the time resolution of the observations from 15 to 1 min resulted in a 320% increase in the estimated ionospheric Joule heating. Such work has not been repeated in the *E* layer.

[7] Auroral electrons precipitating into the atmosphere carry an upward FAC [*Arnoldy*, 1974; *Kamide and Akasofu*, 1976] and lose their energy by collisions at a rate of ~35 eV per ion-electron pair formed [*Rees and Luckey*, 1974]. Upon recombination, ~4% of the deposited energy results in optical emissions associated with the aurora [*Rees and Luckey*, 1974]. The most common visible emissions come from the oxygen atoms, i.e., O(^1D) giving 630 nm in the *F* layer and O(^1S) giving 557.7 nm in the *E* layer. The change in the *E* region plasma density is $n_e \propto \sqrt{I_{5577}}$, where I_{5577} is the 557.7 nm optical intensity, which is directly proportional to the precipitating particle flux [*Kosch et al.*, 2001c]. Hence, the 557.7 nm optical intensity can be used as a proxy to estimate not only the degree of ion-neutral coupling in the *E* layer (see equation (4)) but also the Pedersen conductance [*Kosch et al.*, 1998], which linearly affects Joule heating (see equation (1)). The primary flux of electron energy into the auroral atmosphere is 1–10 keV [*Burch*, 1991]. Optical triangulation has shown that the aurora normally occurs above 100 km altitude [*Currie*, 1955; *Störmer*, 1955]. *Del Pozo et al.* [1997] found that the effective deposition altitude for precipitating electrons in the *E* layer is related to their energy (*E*) by

$$E(H) = 4 \times 10^5 e^{-0.101H} (\mathrm{keV}), \quad (5)$$

where *H* is the altitude in kilometers. Hence, a 557.7 nm aurora at 120 km altitude corresponds to 2.2 keV electrons. The 630 nm aurora corresponds to low-energy electrons precipitating into the *F* region, typically hundreds of eV. By taking intensity ratios of different optical emissions, the energy of the precipitating particles can be estimated [e.g., *Rees and Luckey*, 1974; *Kosch et al.*, 2001c], and therefore, their deposition altitude can be determined.

[8] The upward FAC carried by the precipitating energetic electrons within auroral arcs [*Arnoldy*, 1974; *Kamide and Akasofu*, 1976] must return via an equivalent downward FAC in order to satisfy current continuity, connecting in the ionosphere via Pedersen currents [*Tsunoda et al.*, 1976]. The closing downward current normally appears equatorward (poleward) of the auroral arc in the dusk (dawn) sector, consistent with the large-scale ionospheric electric field associated with ionospheric convection [*Aikio et al.*, 1993; *Armstrong et al.*, 1975; *Lewis et al.*, 1994], although this is not always the case [*Opgenoorth et al.*, 1990]. Normally, the local arc-induced ionospheric electric field enhances the large-scale convection electric field. However, the downward current is carried by cold ionospheric electrons propagating upward [*Arnoldy*, 1974], which leaves a region typically <100 km wide adjacent to the auroral arc, where a plasma depletion of 20%–70% (average 45%) may occur within a minute, though it typically takes 5 min to develop [*Doe et al.*, 1993, 1995]. This results in a similar decrease in the Pedersen conductivity, which is linearly related to the plasma density [*Brekke and Rino*, 1978; *Egeland et al.*, 1973, p. 184]. Hence, in order to satisfy current continuity, intense horizontal ionospheric electric fields, possibly exceeding 100 mV/m, pointing into the auroral arc can develop in a narrow region, possibly <45 km wide, on the equatorward (poleward) side of auroral arcs in the dusk (dawn) sector [*Aikio et al.*, 1993; *Lewis et al.*, 1994; *Opgenoorth et al.*, 1990].

[9] Since the plasma velocity is given by equation (2) and the ion drag component of the neutral velocity is given by equation (3), it is reasonable to expect that the neutral winds should be influenced by the ionospheric electric field associated with auroral arcs. Using a scanning Doppler imager (SDI, similar to that used in the study described in section 2) to distinguish between spatial and temporal variations in the *F* region neutral wind field, *Conde et al.* [2001] found that a latitudinal wind shear was related to an auroral arc in the dusk sector, which they attributed to ion drag. Such an investigation has not been carried out in the *E* layer.

[10] In this study, we investigate the high-latitude *E* region neutral wind field's interaction with auroral arcs at mesoscale spatial resolution during geomagnetically quiet conditions. Two case studies, one each for westward and eastward plasma convection, are presented. The most likely driving mechanism is identified, and the *E* region *e*-folding time is very approximately estimated.

2. Instrumentation and Modeling

[11] Thermospheric neutral winds and temperatures can be derived from passive Doppler measurements of the naturally occurring 630 and 557.7 nm optical emissions in the *F* and *E* layers, respectively, using ground-based FPIs [e.g., *Hernandez*, 1986]. Traditionally, the neutral wind vectors have been derived by scanning the sky at different azimuths at a fixed zenith angle for an assumed altitude, typically close to ~240 and ~120 km for 630 and 557.7 nm, respectively [*Kosch et al.*, 2000a]. This technique is greatly enhanced by the recent development of SDIs, which can derive line-of-sight wind measurements from many tens of software-defined directions simultaneously in a wide field of view [*Conde and Smith*, 1997, 1998]. The information from all line-of-sight Doppler measurements is used to derive an equivalent horizontal wind vector field, assuming that the vertical winds are small [see *Anderson et al.*, 2009, and references therein]. The assumption of small vertical thermospheric winds, especially in the *E* region, is generally valid for quiet geomagnetic conditions [e.g., *Kosch et al.*, 2000b]. In addition, a practical difficulty is that the SDI can only directly measure vertical winds overhead unambiguously, and vertical atmospheric motions are generally not similar within the instrument's field of view [e.g., *Price et al.*, 1995; *Kosch et al.*, 2000b]. Despite this limitation, the SDI is powerful for two reasons: (1) it can differentiate between spatial and temporal ambiguities in the thermospheric neutral wind field and (2) it observes with mesoscale resolution in all directions simultaneously. The typical time resolution of this optical technique is 1–20 min, depending on the emission intensity. The typical spatial resolution is up to 50 and 100 km in the *E* and *F* layers, respectively.

[12] For this study, we employed the Mawson SDI, located in Antarctica [*Anderson et al.*, 2009], to obtain *E* and *F* region neutral winds with mesoscale resolution. Mawson is located at 67.6°S and 62.9°E geographic and 70.4°S and 90.5°E geomagnetic, and magnetic local time =

UT + 1.3. The SDI scanned the etalon gap through one free spectral range in 128 steps in ~50 s. The number of scans integrated is variable depending on the emission intensity, but the software was limited to 1.7–20 min, with an average data cadence of 4 min. The SDI alternated between observations of the 557.7 and 630 nm emissions originating in the *E* and *F* regions, respectively, with the altitude of the former obtained by modeling (discussed in section 3) and that of the latter assumed to be 240 km. The SDI observed 61 unique directions simultaneously in a 144° field of view. The observations were integrated over contiguous azimuthal zones, using zenith angles centered on 0° (1 zone), 23.8° (4 zones), 40.0° (8 zones), 51.8° (12 zones), 60.5° (16 zones), and 67.0° (20 zones). These angles give an approximate radial spacing of 53, 100, 152, 212, and 283 km at 120 km altitude in the *E* region and 105, 200, 305, 425, and 565 km at 240 km altitude in the *F* region.

[13] An all-sky auroral imager was not available at Mawson. Hence, the SDI Doppler fringes were used to produce low-resolution intensity images of the aurora by merging the raw fringe data. Strictly speaking, the pixels of the resulting images are not all precisely at the same wavelength because of spatial variation of the Doppler shift across the field of view, but the change in wavelength is very small, and acceptable images are produced for 557.7 and 630 nm. These images were not calibrated in intensity.

[14] The ionospheric plasma density can be obtained from a frequency-sweeping ionosonde on the basis of the reflection of the HF wave being equal to the plasma frequency as follows:

$$f_{pe}(\mathrm{Hz}) = 9 \times 10^3 \sqrt{n_e(\mathrm{cm}^{-3})}, \tag{6}$$

where n_e is the electron density. The Mawson ionosonde was used to estimate the maximum auroral *E* region electron density. The sounder was swept from 1 to 20 MHz every 5 min. Backscatter direction-of-arrival information was not available, so it was not possible to conclusively determine where the echoes were coming from, which was a limitation during an auroral event.

[15] High-latitude *F* region plasma convection can be derived from the Doppler shift of decameter-scale field-aligned plasma irregularities as observed by the crossed beam HF radar SuperDARN network [*Greenwald et al.*, 1995; *Chisham et al.*, 2007]. The system currently consists of 13 Northern Hemisphere and 6 Southern Hemisphere radars, mostly at high latitudes, and normally has a spatial and temporal resolution of ~50 km and 2 min, respectively. The map potential technique of combining line-of-sight observations [*Chisham et al.*, 2007; *Ruohoniemi and Baker*, 1998] produces plasma velocity vectors where radar data are available as well as large-scale plasma convection equipotential contours. Data from the SuperDARN Southern Hemisphere network of radars were used to generate these outputs with 2 min temporal resolution. This information was used to put the neutral wind case studies into context of the plasma convection. Much of the radar backscatter data come from the Syowa East radar, which overlooks Mawson, so the map potential technique was well constrained near the SDI's field of view.

[16] In this study, the coupled thermosphere ionosphere plasmasphere (CTIP) model [*Fuller-Rowell and Rees*, 1980; *Millward et al.*, 1996] was used to estimate the altitude of the SDI's 557.7 nm observations and to estimate the rotational shear of the neutral wind with altitude in the *E* region. The altitude estimate was done by comparing the SDI's 557.7 nm Doppler temperature measurement with the model prediction. CTIP simulates the time-dependent global structure of the wind vector, temperature, and density of the neutral thermosphere by numerically solving the nonlinear equations of momentum, energy, and continuity on a three-dimensional spherical polar grid rotating with the Earth. The equation of motion includes Coriolis effects, horizontal pressure gradients, horizontal and vertical viscosities, and ion drag. The energy equation describes horizontal and vertical advection of energy, horizontal and vertical heat conduction by both molecular and turbulent diffusion, heating by solar UV and EUV radiation, cooling by infrared radiation, and ionospheric Joule heating. The continuity equation incorporates three major species, namely, atomic oxygen, molecular nitrogen, and molecular oxygen, and includes chemistry, transport, and the mutual diffusion between species. The model latitude, longitude, and time resolutions are 2°, 18°, and 72 min, respectively, and the altitude range spans ~80–1000 km in 15 logarithmically spaced pressure levels. Of course, the CTIP model has neither the spatial nor the temporal resolution to directly model mesoscale auroral features. We use it only to estimate the rotational shear of the steady state neutral wind as a function of altitude, where the model has good spatial resolution.

3. Results and Discussion

[17] We present two case studies of high-latitude *E* region thermospheric winds and their interaction with auroral arcs with mesoscale resolution from Mawson, Antarctica. The selected events took place on 6 June 2008 (day 158, hereafter labeled D158) and 10 June 2008 (day 162, hereafter labeled D162). On D158, K_p = 1 and 2 during the study interval and did not exceed 2^+ for the previous 4 days; that is, quiet geomagnetic conditions prevailed. On D162, $K_p = 0^+$ during the study interval and did not exceed 1^+ for the previous 2 days; that is, very quiet geomagnetic conditions prevailed. Figures 1a–1j and 1k–1t show an overview of the case studies, covering 1600–1900 and 1800–2100 UT on D158 and D162, respectively. Figures 1a and 1k show the IMF data from the ACE satellite with B_z (solid line), B_y (dashed line), and B_x (dotted line) in GSM coordinates. The data have been time lagged by 63 and 73 min on D158 and D162, respectively, to account for the solar wind propagation delay from the ACE satellite. On D158 B_z oscillated around zero with small amplitude, while B_y was mostly negative and B_x was positive. On D162, B_z and B_x were positive throughout, and B_y was mostly negative.

[18] Figures 2a and 2b show the Mawson SDI optical data and Southern Hemisphere SuperDARN radar data, for D158 and D162, respectively. Figures 2a and 2b each consist of time-labeled plots arranged in two groups of three rows. For each group, the top row shows the uncalibrated *F* layer 630 nm Doppler images of intensity across the sky over Mawson, with thermospheric wind vectors (yellow) overlaid for each of the 61 zones; the middle row is in the same

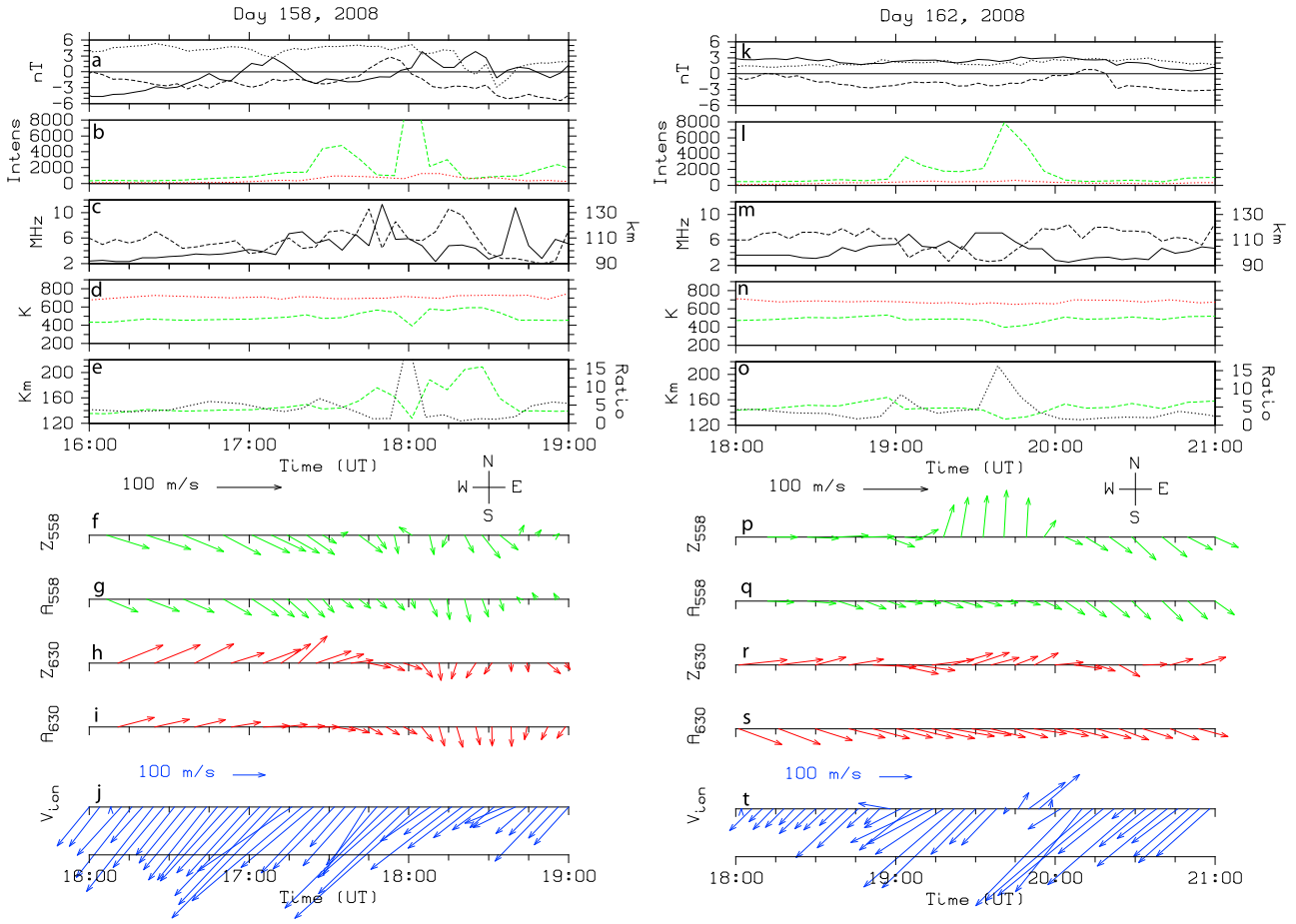

Figure 1. (a–j) An overview of the data for 6 June 2008 (D158). Time is in UT, and the vector directions are geographic. Figure 1a shows the IMF B_z (solid line), B_y (dashed line), and B_x (dotted line) components in GSM coordinates. Figure 1b shows the 630 (red dotted line) and 557.7 nm (green dashed line) uncalibrated optical intensity. Figure 1c shows the *E* region peak plasma frequency (solid line) and the height of the bottom of the *E* layer (dashed line). Figure 1d shows the *F* region (red dotted line) and *E* region (green dashed line) thermospheric neutral temperature. Figure 1e shows CTIP modeled height of the 557.7 nm optical emission (green dashed line) and the optical intensity ratio $I_{630}/I_{557.7}$ (dotted line). Figure 1f shows the *E* region neutral winds (green) for the central sectors out to 24° zenith angle. Figure 1g shows the average *E* region neutral winds (green) for the entire field of view out to 72° zenith angle. Figure 1h shows the *F* region neutral winds (red) for the central sectors out to 24° zenith angle. Figure 1i shows the average *F* region neutral winds (red) for the entire field of view out to 72° zenith angle. Figure 1j shows the average SuperDARN plasma flow vectors (blue) for the entire field of view. Note that the scale for the ion vectors is half that for the wind vectors. (k–t) An overview of the data for 10 June 2008 (D162). The format is identical to that of Figures 1a–1j.

Figure 2. (a) The 144° field-of-view Doppler images of the sky over Mawson. For each group of three rows, the top row show *F* layer 630 nm Doppler images, the middle row shows *E* layer 557.7 nm Doppler images, and the bottom row shows SuperDARN ion convection equipotential contours with 3 kV increments (white) and vectors on 6 June 2008 (D158). Each plot is labeled with UT. The optical intensity is not calibrated. The optical data are plotted in geographic coordinates with wind vectors overlaid for each zone (yellow). The wind vectors are centered on their measurement points. The vector for the zenith sector shows the average wind field, not the vertical wind. The ion convection plots are plotted in geomagnetic coordinates with the SuperDARN vectors (yellow) overlaid at reduced spatial resolution. The large (small) dotted circles represent 70° (80°) geomagnetic south. The SDI's 557.7 nm field of view (green circle) as well as north (blue dot) and east (red dot) geographic directions are overlaid. The ion vectors start on their measurement points. Note that the ion and wind velocity vectors have different scales and shaped vectors for clarity. (b) The format is identical to that of Figure 2a, except it is for 10 June 2008 (D162).

format but for *E* layer 557.7 nm data; and the bottom row shows the large-scale Southern Hemisphere *F* region plasma convection equipotential contours with 3 kV increments (white) and vectors (yellow) obtained from the map potential technique [*Chisham et al.*, 2007; *Ruohoniemi and Baker*, 1998]. The SuperDARN data are synchronized as best as possible with the SDI 557.7 nm plots. The average SDI data cadence was 3.5 and 4.0 min per wavelength on D158 and D162, respectively. The optical plots are orientated in geographic coordinates with north and east to the top and right, respectively. Geomagnetic coordinates are obtained by rotating the axes 44° counterclockwise; that is, geomagnetic north is equivalent to geographic northwest. The optical intensity scale is nonlinear (square root) to accommodate the large intensity range. For the optical data, the vector in the SDI zenith zone shows the average wind field from all

Figure 2

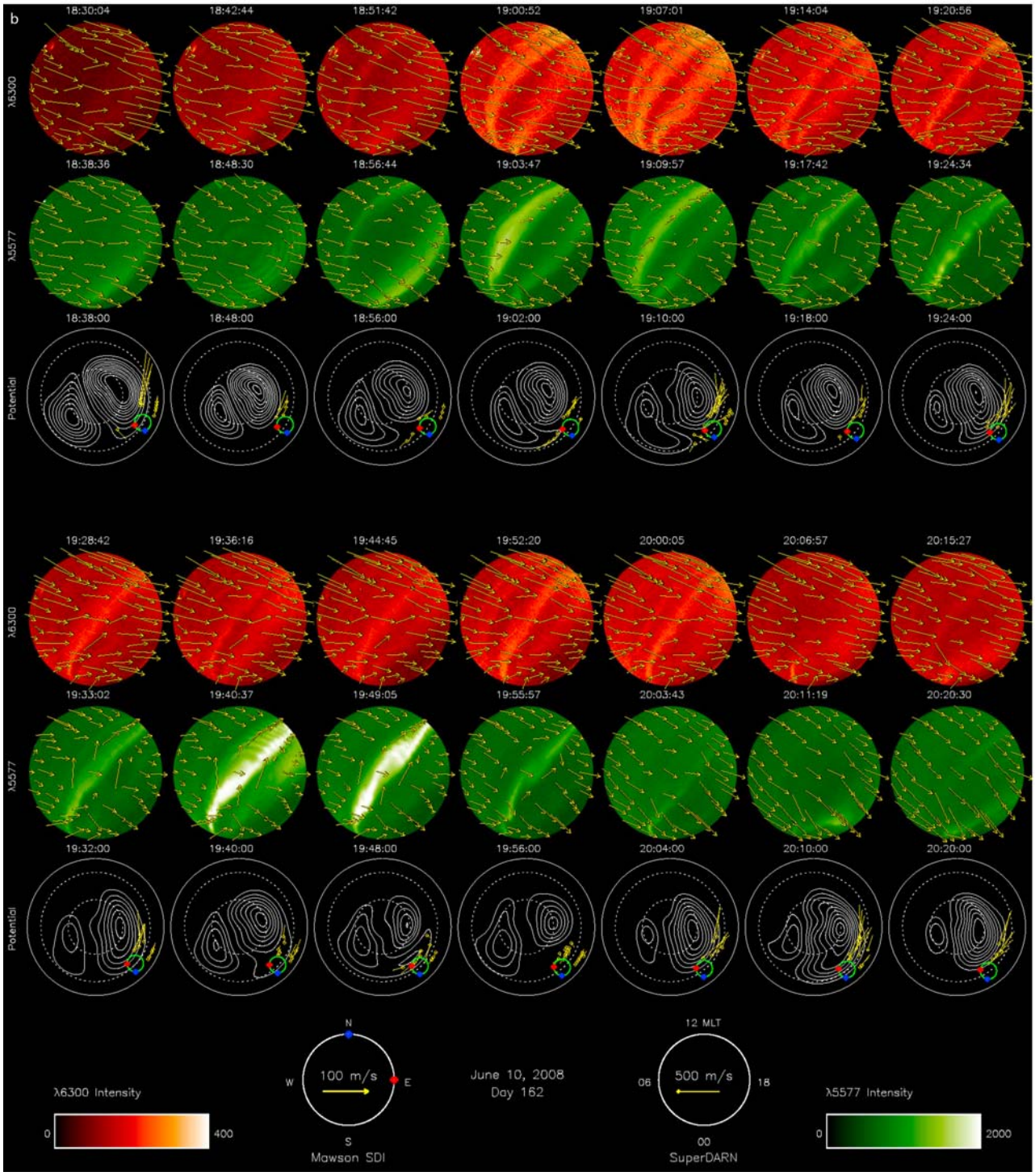

Figure 2. (continued)

measurements, not the vertical wind. This vector essentially represents what a standard FPI would produce from multiple sequential point measurements. The SDI's field of view in the *E* region (green circle) is overlaid onto the SuperDARN plots with geographic north (blue dot) and east (red dot) labeled. The SuperDARN convection plots are orientated in geomagnetic coordinates, so that the Sun is to the top and the dusk (dawn) plasma convection cell is to the right (left). On average, only every third plasma flow vector is shown for clarity. Note that the plasma velocity scale is not the same as that for the neutral wind vectors. The vertical winds over Mawson (not shown) oscillated around zero and showed no particular correlation to the aurora. On D158 (D162), the median 557.7 nm vertical wind speed was 27 (12) m/s, and for 630 nm, it was 25 (18) m/s during the periods of interest. Vertical wind speeds of this magnitude,

oscillating around zero, are common over Mawson, so we are confident that the horizontal wind fit to the SDI Doppler data is good.

[19] For D158 (Figure 2a), the upper and lower thermospheric winds flowed eastward and southeastward at the start of this event, consistent with the work of *Anderson et al.* [2009]. As is clearly evident from the optical images, an auroral arc appeared at ~1721:42 UT in the southeast (geomagnetic poleward) and progressed toward the northwest (geomagnetic equatorward). Notable in the 557.7 nm data from 1727:52 to 1754:19 UT is that poleward of the arc, the winds decreased in amplitude, whereas equatorward of the arc, the winds remained unaffected. The 630 nm winds appear mostly unaffected by the arc's passage. However, from 1754:19 UT onward the 557.7 nm winds northeast (geomagnetic east) of Mawson rotated essentially 90° to flow southwestward (geomagnetic west) parallel to the arc within a region ~50 km wide on either side of the arc. This was very clear at 1801:24 UT. However, this rotation was localized and did not occur southwest of Mawson. The 630 nm winds only started to respond to the aurora from 1804:37 UT onward, when they also rotated to flow parallel to the arc. Again, the neutral flow is toward the southwest (geomagnetic west) but is localized to the northeast (geomagnetic east) of Mawson. Few SuperDARN data were available on D158, but the majority came from the Syowa East radar with backscatter to the geomagnetic west of Mawson. Hence, the plasma flow equipotential contours are reliable near Mawson. The SuperDARN data clearly show that Mawson was under the dusk plasma convection cell and experienced geomagnetic westward plasma flow in the *F* region throughout this event. The large-scale two-cell plasma convection circulation in the *F* layer is consistent with the observed B_z, and B_y negative enhanced the size of the dawn convection cell. Importantly for this event, not only were the lower thermospheric winds significantly affected by the passage of the arc, but both upper and lower thermospheric winds rotated to flow parallel to the arc in the direction of the plasma flow.

[20] For D162 (Figure 2b), the upper and lower thermospheric winds flowed primarily eastward (geomagnetic southeastward) at the start of this event, consistent with the work of *Anderson et al.* [2009]. From 1903:17 to 1955:57 UT, an auroral arc appeared over Mawson, reaching its peak intensity between 1940:37 and 1949:05 UT. Notable in the 557.7 nm data from 1909:57 to 1955:57 UT is that the neutral wind in the *E* layer rotated 90° to flow northeastward (geomagnetic eastward), i.e., parallel to the arc, within a region ~50 km wide on either side of the arc. This observation is consistent with that of *Wescott et al.* [2006], who also found the *E* region neutral wind to be parallel to an auroral arc from a rocket chemical release experiment. Elsewhere in the SDI's field of view, i.e., geomagnetic poleward and equatorward of the arc, the wind field remained unchanged from the previous background flow. From 2003:43 UT onward, the arc disappeared, and the *E* region winds rotated back, so that the neutral flow was eastward and southeastward in the upper and lower thermosphere, respectively, i.e., as if the auroral arc had never existed. The slow rotation of the 557.7 nm background winds from eastward to southeastward over 2 h is expected at this time and is consistent with the large-scale plasma convection pattern. The 630 nm winds appear largely unaffected by the arc's passage. However, from 1914:04 to 1952:20 UT there is some evidence that the *F* region winds also rotated to flow northeastward parallel to the arc. However, this rotation was localized and only occurred overhead and southwest of Mawson. Similar to the 557.7 nm winds, the 630 nm winds rotated back to flow eastward when the arc disappeared. This event is different from D158 because it shows that the winds rotate to flow in the direction opposite to what might be expected in the dusk sector plasma flow, i.e., geomagnetically eastward instead of westward. However, the IMF B_z and B_y were positive and mostly negative, respectively, throughout this event (Figure 1k), thereby making large-scale multicell plasma convection in the *F* layer possible with an enhanced dawn cell. Again, few SuperDARN data were available on D162, the majority coming from the Syowa East radar with backscatter mostly (sometimes) to the geomagnetic west (east) of Mawson. Hence, again, the plasma flow equipotential contours are reliable near Mawson. The SuperDARN data show that Mawson was in fact under (e.g., 1948 UT) or near (e.g., 1910 UT) the dawn plasma convection cell, which was greatly extended into the dusk sector and therefore experienced geomagnetic eastward plasma flow in the *F* region. Although the SuperDARN data show that between 1910 and 1948 UT, Mawson was under geomagnetic westward plasma flow, the continued northeastward wind parallel to the arc presumably comes about because of the high inertia of the neutral atmosphere in the *E* region. Prior to and after this event, Mawson was under geomagnetic westward plasma flow, as is normally expected for the dusk sector. For this event, the upper thermospheric winds were largely unaffected by the passage of the arc, but the lower thermospheric winds rotated to flow parallel to the arc in the direction of the plasma flow. While the geomagnetic eastward plasma flow direction was unusual for the time of day (i.e., dusk sector), the wind rotation on D162 was consistent with D158.

[21] Figures 1b and 1l show the 630 (red dotted line) and 557.7 nm (green dashed line) uncalibrated optical intensity averaged over a cone of ±32° zenith angle from the SDI Doppler images. The passage of the 557.7 nm auroral arcs is clearly seen on both days, peaking at 14,200 and 7900 counts on D158 (Figure 1b) and D162 (Figure 1l), respectively. The 630 nm intensity is much lower and less variable than the 557.7 nm emission, as expected, peaking at 1300 and 650 counts on D158 and D162, respectively. Figures 1c and 1m show the estimated *E* region peak plasma frequency (solid line) and height of the bottom of the peak (dashed line) extracted from ionograms. The auroral *E* layer blanketed the *F* region for most of the time. The wide field of view of the ionosonde and the complex nature of auroral precipitation on D158 make the exact geographic location of the plasma frequency data uncertain. However, the increase in peak *E* region frequency during each event, compared with immediately before and after the event, is clear. On D158 and D162, the peak *E* region frequency went from 2.3 to 11.3 (corresponding to 6.5×10^4 and 1.6×10^6 el/cm^3) and from 3.1 to 7.1 MHz (corresponding to 1.2×10^5 and 6.2×10^5 el/cm^3), respectively. From equation (6), this represents a 24.1X and 5.2X increase in plasma density on D158 and D162, respectively. The altitude of the bottom of the auroral *E* layer on D158 occurred between 90 and

133 km but was very variable. According to equation (5), this corresponds to precipitating electrons of energy >0.5 keV. Off-vertical ionosonde reflections from auroral *E* layers will give an apparent height greater than the actual height. Hence, when the height measurements are variable, the bottom of the *E* layer is likely to be closer to the lower measured height, which also increases the electron energy estimate. On D162 the altitude varied more smoothly from 93 to 123 km, corresponding to electron energies >1.6 keV, reaching a minimum height when the auroral arc was overhead. The decrease in altitude indicates a hardening of the precipitating electron energy spectrum [*del Pozo et al.*, 1997].

[22] Figures 1d and 1n show the *F* region (red dotted line) and *E* region (green dashed line) thermospheric neutral temperature averaged over a cone of ±32° zenith angle from the SDI Doppler data. The upper thermospheric temperature varied from 670 to 740 K and from 650 to 700 K on D158 and D162, respectively. These modest temperatures in the *F* region are consistent with solar minimum. The lower thermospheric temperature varied from 430 to 580 K and from 400 to 530 K on D158 and D162, respectively. Note that the 557.7 nm Doppler temperature dropped noticeably during the passage of the bright auroras. This we associated with a drop in the 557.7 nm emission altitude [e.g., *Holmes et al.*, 2005], and it is consistent with the ionosonde data. Figures 1e and 1o show the optical intensity ratio I_{5577}/I_{6300} (dotted line) from Figures 1b and 1l and the CTIP modeled height of the 557.7 nm optical emission (green dashed line) inferred from the SDI temperature observations in Figures 1d and 1n. The ratio of optical intensities is a useful indicator of the energy of precipitating electrons [e.g., *Rees and Luckey*, 1974], although our uncalibrated data do not allow us to make a quantitative estimate. However, it is clear that during the passage of the auroral arcs, seen in Figures 1b and 1l, the intensity ratio increases, peaking at 23.0 and 16.4 on D158 and D162, respectively. An increased intensity ratio indicates a hardening of the electron energy spectrum, which would be associated with a decrease in the emission altitude [e.g., *del Pozo et al.*, 1997]. This predicted behavior is clearly shown by the CTIP modeled height of the 557.7 nm emission, decreasing in altitude as the auroral arcs pass overhead of Mawson (see Figures 1e and 1o) and is consistent with the ionosonde data (Figures 1c and 1m). On D158 and D162, the modeled altitude of the 557.7 nm emission varies from 128 to 209 km and from 130 to 164 km, respectively.

[23] Figure 1 also shows the SDI *E* region neutral winds averaged over a cone of ±32° zenith angle (Z_{558}) (Figures 1f and 1p) and the entire field of view (A_{558}) (Figures 1g and 1q). The vectors are shown in geographic coordinates. For D158, there was little apparent difference between narrow and wide fields of view, except at ~1730 and ~1800 UT, when the winds near the zenith acquired a small northward meridional component as the aurora appeared (Figure 1b). For D162, there was a clear difference between the narrow and wide fields of view. The 557.7 nm winds near the zenith became strongly northward between 1915 and 2000 UT. These data clearly demonstrate the power of the all-sky SDI versus traditional FPIs in separating spatial versus temporal ambiguities at mesoscale resolution. Also shown are the SDI *F* region neutral winds averaged over a cone of ±32° zenith angle (Figures 1h and 1r) and the entire field of view (Figures 1i and 1s). For D158, there was little apparent difference between narrow and wide fields of view, except prior to ~1745 UT, the winds near the zenith had a larger amplitude and a greater northward meridional component. For D162, there was a clear difference between the narrow and wide fields of view. The 630 nm winds near the zenith had a northward meridional component for much of the time, whereas the average wind field always had a southward meridional component.

[24] Figures 3a and 3b show the CTIP modeling outcome for 1800 UT on D158 and 1912 UT on D162, respectively, the model times closest to the appearance of the auroral arcs. Figure 3 shows the altitude profile for neutral temperature (green solid line) and meridional (dotted line) and zonal (dashed line) winds in geographic coordinates, where north and east are positive. This modeling exercise is necessary in order to determine whether the observed wind rotations, seen in Figure 2, associated with auroral arcs in the *E* region could be due to wind shear in altitude. The temperature profile is that which was used to estimate the 557.7 nm emission altitude in Figures 1e and 1o. On D158, the estimated altitude varies from 128 to 209 km, giving a CTIP meridional wind component from −26.6 to 20.2 m/s northward and a zonal component from −100.7 to −80.0 m/s eastward, respectively. At 128 and 209 km altitude, this corresponds to a wind of amplitude 104.2 and 82.5 m/s and a direction of 255.2° and 284.2° geographic, respectively, measured east of geographic north. CTIP predicts that the *E* region wind is predominantly westward, which is very different from what the SDI observed (see Figures 1f and 1g). However, *Anderson et al.* [2009] found a similar discrepancy between observations and CTIP at Mawson. Likewise, *Kosch et al.* [2000a] also found systematic differences between observations and the CTIP model in the northern high-latitude hemisphere. More importantly, the change in altitude brings a change in wind direction of ~29°, which is too small to explain the SDI observations of ~90° rotation. Following the same procedure for D162, the estimated altitude varies from 130 to 164 km, giving a CTIP meridional wind component from −28.3 to −57.8 m/s northward and a zonal component from −93.4 to −95.9 m/s eastward, respectively. At 130 and 164 km altitude, this corresponds to a wind of amplitude 97.6 and 112 m/s and direction of 253.1° and 238.9° geographic, respectively. CTIP predicts that the *E* region wind is predominantly southwestward, which is again very different from what the SDI observed (see Figures 1p and 1q). However, the change in altitude only brings a change in wind direction of ~14°, which is again far too small to explain the SDI observations of ~90° rotation. Hence, we conclude that the wind rotation observed by the SDI in the vicinity of the auroral arcs is real and not an artifact of the 557.7 nm emission altitude changing.

[25] Figures 1j and 1t show the average SuperDARN plasma flow vectors (blue) in the *F* region for the entire SDI field of view. The data are plotted at 4 min resolution for clarity. Note that the scale for the plasma vectors is half that for the neutral wind vectors. The number and location of SuperDARN data were variable and generally not overhead of Mawson (see Figures 2a and 2b). On both days, SuperDARN almost never had data within a 200 km radius of Mawson. The maximum number of plasma vectors at any

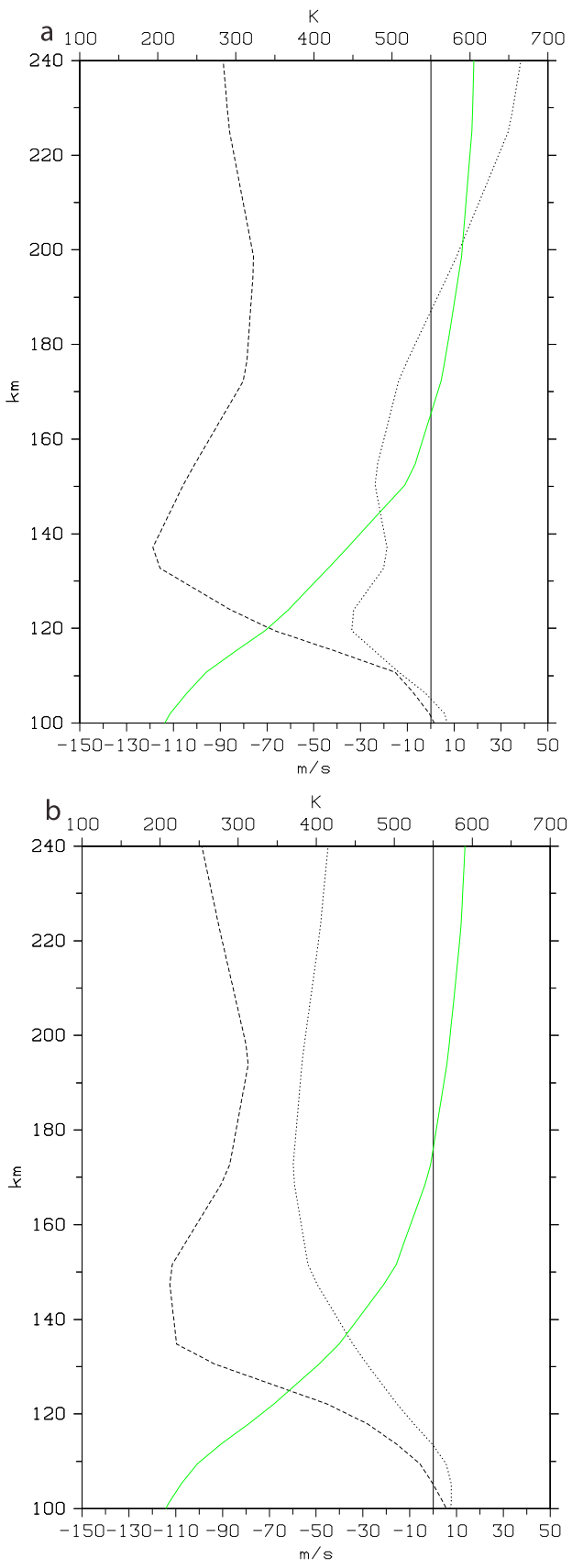

one time within the SDI's *F* region field of view was 14 during both events with an average geomagnetic location of 69.0°S, 81.5°W on D158 and 69.0°S, 80.4°W on D162. This corresponds to an average distance of 380 and 419 km slightly north of geomagnetic west from Mawson on D158 and D162, respectively, i.e., near the edge of the SDI's *F* region field of view. These distances translate to Mawson being 36.0 and 40.4 min ahead of the SuperDARN data on D158 and D162, respectively. As a result of this spatial discrepancy only a general qualitative comparison of plasma and neutral wind vectors is possible. However, such a comparison remains valid because the auroral arcs were geomagnetically east–west aligned. On both D158 and D162, the general background plasma flow is southwest (geomagnetic westward), as expected for the dusk sector. On D158, the passage of the auroral arc at ~1730 and ~1800 UT corresponds to an increase in the plasma flow in the same direction as the background flow. This is entirely consistent with the expected ionospheric electrodynamics of an auroral arc [e.g., *Aikio et al.*, 1993; *Lewis et al.*, 1994; *Opgenoorth et al.*, 1990]. However, on D162, the appearance of the auroral arc at ~1900 UT resulted in westward plasma flow, and at ~1945 UT, it resulted in northeastward (geomagnetic eastward) plasma flow, the latter being in the direction opposite to the expected plasma flow in the dusk sector. However, as Figure 2b shows, Mawson was temporarily under the dawn plasma convection cell around 1856 to 1902 UT as well as 1948 and 1956 UT. The dawn convection cell had extended itself into the dusk sector during this event, consistent with persistent B_z positive. Although this scenario is somewhat unusual, the SDI observations remain consistent with the expected ionospheric electrodynamics of an auroral arc, as described in section 1.

[26] It seems clear that the two normally dominant driving forces for neutral winds in the *E* region, namely, solar heating and Coriolis force, are not responsible for the mesoscale change in wind pattern associated with auroral arcs. First, the solar heating pressure force would be fairly constant throughout the studied events. Second, if Joule heating associated with the auroral arc caused the gas to expand perpendicularly away from the arc, the Coriolis force would act in opposite directions on either side of the arc, which is not the case. The observations show the wind blowing parallel to the arc in the same direction on both sides of the arc. The CTIP model shows that the change in emission altitude is not sufficient to explain the observed rotation of neutral wind vectors. The most likely candidate force to explain the observations appears to be ion drag, which is in the correct direction for both events. Since the plasma density increases by 24.1X on D158 and 5.2X on D162, equation (4) shows that the ion-neutral coupling time decreases by the same amount. It is shown on D158 that the vector rotation occurred within one time step, i.e., 7 min, consistent with the large increase in *E* region plasma density of 24.1X. Furthermore, D162 shows that the vector rotation occurred within two time

Figure 3. (a) CTIP model altitude profile for neutral temperature (green solid line), meridional (dotted line), and zonal (dashed line) winds at 1800 UT on 6 June 2008 (D158). (b) The format is identical to that of Figure 3a, except it is for 10 June 2008 (D162).

steps, i.e., 16 min, consistent with the smaller plasma density enhancement of 5.2X. Hence, we conclude that the ion drag *e*-folding time in the *E* region can be very short, of the order of 10 min or less, depending on the plasma density. Unfortunately, the lack of plasma flow data in the *E* region and the low SDI data cadence do not permit a proper quantitative assessment of the *E* region *e*-folding time for these data.

[27] For an auroral arc in the dusk (dawn) sector, the poleward (equatorward) pointing ionospheric electric field on the equatorward (poleward) side of the auroral arc, associated with the closure of the FAC within and near the arc, provides the driving $\mathbf{E} \times \mathbf{B}$ force for the ions, which then accelerate the neutral gas in the observed directions via collisions. Unfortunately, the temporal resolution of the 557.7 nm SDI data is too low to resolve on which side of the arc the winds rotated because the arcs are moving in the geomagnetic meridional direction. However, our observations strongly suggest that the increased ion drag must be sufficient to overcome the other existing forces acting on the neutral particles. Without a suitable radar, such as the European Incoherent Scatter (EISCAT) facility, we have no means of estimating mesoscale plasma flow in the *E* region and therefore no means of direct verification at this time.

[28] The time interval 1910 to 1940 UT on D162 provides an interesting observation. For ~15 min prior to 1910 UT and after 1940 UT, *F* region plasma flow near Mawson was eastward geomagnetic close to, and presumably within, the SDI field of view (see Figure 2b), which is consistent with the argument given above for the neutral wind direction adjacent to the auroral arc. However, beginning at 1910 UT and continuing until 1940 UT, the dominant *F* region plasma flow was in the geomagnetic westward direction; yet the neutral winds remained eastward adjacent to the arc. Earlier we stated that this was due to the considerable inertia of the *E* region atmosphere, but the *E* region *e*-folding time for D162 was then estimated to be <16 min, which is much shorter than the 30 min of opposite *F* region plasma and *E* region neutral flow. During this interval the auroral arc became brighter, suggesting an increased FAC strength and therefore also an increased arc-induced ionospheric electric field. The ionosonde data (Figure 1m) show the *E* region plasma density increasing, so ion-neutral coupling was also increasing. Therefore, one might expect the neutral winds parallel to the arc to reverse direction at ~1910 and ~1940 UT, but this is not what the SDI observations show. Hence, it may be true that once the region of downward FAC associated with the arc is established according to the large-scale plasma flow [*Aikio et al.*, 1993; *Armstrong et al.*, 1975; *Lewis et al.*, 1994], in this case equatorward of the arc, it cannot suddenly switch to the other side of the arc because the plasma convection has reversed itself. This would be consistent with the observation of *Opgenoorth et al.* [1990] that the side of the arc where the closure FAC flows is not always consistent with the large-scale ionospheric convection electric field. To the authors' best knowledge, our observation may be unique. If true, this implies that the local *E* region plasma flow associated with the arc is in the direction opposite to the background *F* region plasma flow. Unfortunately, we are unable to verify the above speculation properly for lack of spatially coincident SDI and SuperDARN observations.

[29] Finally, we find that there are no noticeable changes in the *E* or *F* region neutral temperature adjacent to the arc for either D158 or D162. This is perhaps surprising given that ion drag, i.e., ion-neutral collisions, is assumed responsible for the wind rotation adjacent to the arc. However, the hardening of the precipitating electron spectrum caused the 557.7 nm emission altitude to descend, which caused an apparent decrease in *E* region temperature. The Pedersen conductivity peaks at 120 km in the lower *E* region [*Schlegel*, 1988], and so Joule heating (see equation (1)) in the *F* region is expected to be lower by approximately an order of magnitude. However, although the Joule heat dissipation per unit volume is higher in the *E* region, the rate of heating per unit mass is greatest around 400 km [*Deng and Ridley*, 2007], so the temperature change in the *F* region should be greater. Since the SDI data show no significant thermospheric temperature change, we conclude that Joule heating was very low, consistent with $K_p <= 2$ during these events [*Kosch and Nielsen*, 1995].

[30] It is clear that the neutral wind in the high-latitude *E* region can be strongly influenced by auroral precipitation in the form of arcs. This requires that the two following conditions be met: (1) the energy of the precipitating particles is high enough for a plasma density enhancement to occur in the *E* layer [e.g., *del Pozo et al.*, 1997] and (2) the flux is high enough to cause appreciable enhancement in the plasma density [e.g., *Kosch et al.*, 1998]. The particle energy and flux can be estimated from calibrated optical intensity ratios [e.g., *Rees and Luckey*, 1974]. If both the energy and flux are high enough, then the *E* region plasma density is enhanced, as is frequently the case for auroral arcs. This then linearly increases the ion-neutral coupling or, in other words, linearly reduces the coupling *e*-folding time (see equation (4)). The flux of auroral particles is also a measure of the upward current flowing within the auroral arc, which has to be matched by an equal downward current. This pair of FAC sheets must be closed in the ionosphere by a horizontal Pedersen current with its associated electric field. This electric field produces a localized plasma flow via the $\mathbf{E} \times \mathbf{B}$ force, which then creates the necessary ion drag to force the neutral wind flow in another direction, i.e., parallel to the arc. *Wang et al.* [2005] found that the nightside FAC behaved like a current source. *Vickrey et al.* [1986] showed that the magnetosphere acts as a current generator on a 3–80 km spatial scale. Hence, the ionospheric electric field is a function of the *E* region Pedersen conductance, which is linearly dependent on the plasma density and can be estimated from calibrated 557.7 nm optical data [*Kosch et al.*, 1998; *Senior et al.*, 2008]. The plasma density adjacent to the auroral arc is reduced because the downward return current is carried by cold ionospheric electrons, and so an intense electric field can develop adjacent to arcs on one side, especially if they remain stationary long enough (several minutes) to create a plasma density depletion [*Doe et al.*, 1993, 1995]. However, it is the enhanced plasma density of the arc that produces the enhanced ion-neutral coupling, seemingly opposite to the need to generate a strong ionospheric electric field. Hence, a balance must exist in plasma density between the need to generate a strong ionospheric electric field (i.e., low plasma density) and the need to generate strong ion-neutral coupling (i.e., high plasma density). The high (low) ionospheric plasma density region

will be within (next to) the arc, spatially separated by a few tens of kilometers. Presumably, both conditions of a strong electric field and high ion-neutral coupling can be more easily met by having a strong particle flux, i.e., a bright aurora, and the arc slowly drifting perpendicular to its long axis. Both conditions occur frequently for auroral arcs. The phenomenon described here would not necessarily apply to other types of aurora (e.g., pulsating patches) because it is not obvious that all the necessary conditions (e.g., enhanced ionospheric electric field) would be satisfied.

[31] This study can be improved in a quantitative sense in the following three regards:

[32] 1. The SDI data cadence in the *E* region was too slow, averaging 7–8 min, to observe the *E* region neutral wind response time in the vicinity of the auroral arc, limited partly by the scanning etalon speed, minimum integration time imposed, and interleaved 630 nm observations. Increasing the data cadence may also reveal the wind rotation occurring only on one side of the arc, as expected.

[33] 2. The SDI spatial resolution can be improved by adjusting the data zones to permit a resolution better than 50 km.

[34] 3. The availability of simultaneous electric field and plasma density data in the *E* region would permit quantitative calculation of the ion-neutral *e*-folding time as a function of plasma density. It would also permit estimation of the neutral wind-corrected Joule heating [e.g., *Kosch and Nielsen*, 1995] and FAC strength [e.g., *Kosch et al.*, 2001b] in the vicinity of the auroral arc, both of which indirectly affect the ion drag. In the *F* layer, the neutral wind can affect the Joule heating by as much as 60% [*Cierpka et al.*, 2000]. However, ionospheric Joule heating is primarily an *E* region phenomenon, yet the effect of the neutral wind field has to date not been properly quantified through observations. The *E* region Hall [*Senior et al.*, 2007] and Pedersen [*Kosch et al.*, 1998] conductance data can be obtained from calibrated riometer absorption and 557.7 nm optical data, respectively. In addition, incoherent scatter radar data [*Kirkwood and Osepian*, 1995], or multiwavelength calibrated optical data [e.g., *Rees and Luckey*, 1974], will allow the characteristic energy and flux of the precipitating particles to be determined. This, in turn, will give altitude and FAC strength of the auroral arc [e.g., *del Pozo et al.*, 1997], which then determines the degree of ion-neutral coupling in the *E* layer close to the arc. Steerable radar systems such as the EISCAT facility are capable of providing interleaved *E* and *F* region tristatic plasma velocity, density, and temperature measurements with acceptable temporal resolution [e.g., *Davies et al.*, 1997; *Makarevich et al.*, 2006].

4. Conclusion

[35] We have shown, for the first time, that auroral precipitation in the form of arcs can have a dramatic effect on the *E* region neutral wind field on a spatial mesoscale. Using an SDI, two effects are observed: (1) A magnetically equatorward moving arc caused the wind speed to rapidly diminish poleward of the arc. (2) An auroral arc caused the wind direction to rotate 90° to flow parallel to the arc within 7–16 min in a region less than ~50 km from the arc. We show that this effect is due neither to changing altitude of the emission nor to the normally dominant solar heating pressure and Coriolis forces in the *E* region but that increased plasma density and electric field in the immediate vicinity of the auroral arc greatly enhances the localized ion drag forces, possibly by more than an order of magnitude.

[36] **Acknowledgments.** Operation of the Southern Hemisphere SuperDARN radars is supported by the national funding agencies of Australia, France, Japan, South Africa, and the United Kingdom. The CTIP model was run through the Community Coordinated Modelling Centre (http://ccmc.gsfc.nasa.gov). IMF data are supported by the NASA/ACE program. The Mawson ionosonde is operated by the Ionospheric Prediction Service (IPS) of Australia (http://www.ips.gov.au/). This research has been supported by the Australian Research Council's Discovery Projects DP0557369 and DP0770366 and by the Australian Antarctic Science Program. M.J.K. acknowledges support from the Institute of Advanced Study at La Trobe University, Melbourne, Australia.

[37] Wolfgang Baumjohann thanks Mamoru Ishii and another reviewer for their assistance in evaluating this paper.

References

Aikio, A. T., et al. (1993), Ground-based measurements of an arc-associated electric field, *J. Atmos. Terr. Phys.*, *55*, 797–808.

Anderson, C., et al. (2009), Thermospheric winds and temperatures above Mawson, Antarctica, observed with an all-sky imaging Fabry-Perot spectrometer, *Ann. Geophys.*, *27*, 2225–2235.

Armstrong, J. C., et al. (1975), A comparison of satellite observations of Birkeland currents with ground observations of visible aurora and ionospheric currents, *J. Geophys. Res.*, *80*, 575–586.

Arnoldy, R. L. (1974), Auroral particle precipitation and Birkeland currents, *Rev. Geophys.*, *12*, 217–231.

Aruliah, A. L., and E. Griffin (2001), Evidence of meso-scale structure in the high-latitude thermosphere, *Ann. Geophys.*, *19*, 1–10.

Aruliah, A. L., et al. (1991), The combined effect of solar and geomagnetic activity on high latitude thermospheric neutral winds. Part I: Observations, *J. Atmos. Terr. Phys.*, *53*, 467–483.

Aruliah, A. L., et al. (2004), First tristatic studies of meso-scale ion-neutral dynamics and energetics in the high-latitude upper atmosphere using collocated FPIs and EISCAT radar, *Geophys. Res. Lett.*, *31*, L03802, doi:10.1029/2003GL018469.

Aruliah, A. L., et al. (2005), First direct evidence of meso-scale variability on ion-neutral dynamics using co-located tristatic FPIs and EISCAT radar in Northern Scandinavia, *Ann. Geophys.*, *23*, 147–162.

Brekke, A., and C. L. Rino (1978), High-resolution altitude profiles of the auroral zone energy dissipation due to ionospheric currents, *J. Geophys. Res.*, *83*, 2517–2524.

Burch, J. L. (1991), Diagnostics of auroral acceleration mechanisms by particle measurements, in *Auroral Physics*, edited by C.-I. Meng, M. J. Rycroft, and L. A. Frank, pp. 97–107, Cambridge Univ. Press, New York.

Chisham, G., et al. (2007), A decade of the Super Dual Auroral Radar Network (SuperDARN): Scientific achievements, new techniques and future directions, *Surv. Geophys.*, *28*, 33–109, doi:10.1007/s10712-007-9017-8.

Cierpka, K., et al. (2000), Ion-neutral coupling in the high-latitude F-layer from incoherent scatter and Fabry-Perot interferometer measurements, *Ann. Geophys.*, *18*, 1145–1153.

Codrescu, M. V., et al. (2000), Electric field variability associated with the Millstone Hill electric field model, *J. Geophys. Res.*, *105*, 5265–5273.

Conde, M., and R. W. Smith (1997), Phase compensation of a separation scanned, all-sky imaging Fabry-Perot spectrometer for auroral studies, *Appl. Opt.*, *36*, 5441–5450.

Conde, M., and R. W. Smith (1998), Spatial structure in the thermospheric horizontal wind above Poker Flat, Alaska, during solar minimum, *J. Geophys. Res.*, *103*, 9449–9471.

Conde, M., et al. (2001), Assimilated observations of thermospheric winds, the aurora, and ionospheric currents over Alaska, *J. Geophys. Res.*, *106*, 10,493–10,508.

Crickmore, R. I. (1995), A study of the thermospheric forces at a high latitude site on two days of differing geomagnetic activity, *J. Atmos. Terr. Phys.*, *57*, 759–773.

Currie, B. W. (1955), Auroral heights over west-central Canada, *Can. J. Phys.*, *33*, 773–779.

Davies, J. A., et al. (1997), Deriving the normalised ion-neutral collision frequency from EISCAT observations, *Ann. Geophys.*, *15*, 1557–1569.

del Pozo, C. F., et al. (1997), Ion composition and effective ion recombination rate in the nighttime auroral lower ionposphere, *J. Atmos. Sol. Terr. Phys.*, *59*, 1919–1943.

Deng, Y., and A. J. Ridley (2007), Possible reasons for underestimating Joule heating in global models: E field variability, spatial resolution, and vertical velocity, *J. Geophys. Res.*, *112*, A09308, doi:10.1029/2006JA012006.

Doe, R. A., et al. (1993), Observations of nightside auroral cavities, *J. Geophys. Res.*, *98*, 293–310.

Doe, R. A., et al. (1995), Electrodynamic model for the formation of auroral ionospheric cavities, *J. Geophys. Res.*, *100*, 9683–9696.

Egeland, A., et al. (1973), *Cosmical Geophysics*, Universitetsforlaget, Oslo.

Friis-Christensen, E., et al. (1985), Interplanetary magnetic field control of the high-latitude electric fields and currents determined from Greenland magnetometer data, *J. Geophys. Res.*, *90*, 1325–1338.

Fuller-Rowell, T. J., and D. Rees (1980), A three dimensional time dependent model of the thermosphere, *J. Atmos. Sci.*, *37*, 2545–2567.

Galperin, Y. I. (2001), Multiple scales in auroral plasmas, *J. Atmos. Sol. Terr. Phys.*, *64*, 211–229.

Greenwald, R. A., et al. (1995), DARN/SuperDARN: A global view of the dynamics of high-latitude convection, *Space Sci. Rev.*, *71*, 761–796.

Heelis, R. A., et al. (2002), Ion and neutral motions observed in the winter polar upper atmosphere, *J. Geophys. Res.*, *107*(A12), 1476, doi:10.1029/2002JA009359.

Hernandez, G. (1986), *The Fabry-Perot Interferometer*, Cambridge Univ. Press, New York.

Holmes, J. M., et al. (2005), Morphology of evening sector aurorae in λ557.7-nm Doppler temperatures, *Geophys. Res. Lett.*, *32*, L02103, doi:10.1029/2004GL021553.

Iijima, T., and T. A. Potemra (1976), The amplitude distribution of field-aligned currents at northern high latitudes observed by triad, *J. Geophys. Res.*, *81*, 2165–2174.

Iijima, T., and T. Shibaji (1987), Global characteristics of northward IMF-associated (NBZ) field-aligned currents, *J. Geophys. Res.*, *92*, 2408–2424.

Kamide, Y., and S.-I. Akasofu (1976), The location of the field-aligned currents with respect to discrete auroral arcs, *J. Geophys. Res.*, *81*, 3999–4003.

Killeen, T. L., and R. G. Roble (1984), An analysis of the high-latitude thermospheric wind pattern calculated by a thermospheric general circulation model: 1. Momentum forcing, *J. Geophys. Res.*, *89*, 7509–7522.

Killeen, T. L., and R. G. Roble (1986), An analysis of the high-latitude thermospheric wind pattern calculated by a thermospheric general circulation model: 2. Neutral parcel transport, *J. Geophys. Res.*, *91*, 11,291–11,307.

Killeen, T. L., and R. G. Roble (1988), Thermospheric dynamics: Contributions from the first 5 years of the Dynamics Explorer program, *Rev. Geophys.*, *26*, 329–367.

Kirkwood, S., and A. Osepian (1995), Quantitative studies of energetic particle precipitation using incoherent scatter radar, *J. Geomagn. Geoelectr.*, *47*, 783–799.

Knudsen, D. J., et al. (2001), Width and structure of mesoscale optical auroral arcs, *Geophys. Res. Lett.*, *28*, 705–708.

Kosch, M. J., and E. Nielsen (1995), Coherent radar estimates of average high-latitude ionospheric Joule heating, *J. Geophys. Res.*, *100*, 12,201–12,215.

Kosch, M. J., and E. Nielsen (2001), Coherent radar estimates of high latitude field-aligned currents: statistical averages, *Adv. Space Res.*, *27*(6–7), 1239–1244.

Kosch, M. J., et al. (1998), Extrapolating EISCAT height-integrated Pedersen conductivities to other parts of the sky using ground-based auroral images, *Ann. Geophys.*, *16*, 583–588.

Kosch, M. J., et al. (2000a), A comparison of thermospheric winds and temperatures from Fabry-Perot interferometers and EISCAT radar measurements with models, *Adv. Space Res.*, *26*, 979–984.

Kosch, M. J., et al. (2000b), A comparison of vertical thermospheric winds from Fabry-Perot interferometer measurements over a 50 km baseline, *Adv. Space Res.*, *26*(6), 985–988.

Kosch, M. J., et al. (2001a), High-latitude ground-based observations of the thermospheric ion-drag time constant, *Geophys. Res. Lett.*, *28*, 1395–1398.

Kosch, M. J., et al. (2001b), The importance of conductivity gradients in ground-based field-aligned current studies, *Adv. Space Res.*, *27*(6–7), 1277–1282.

Kosch, M. J., et al. (2001c), High resolution maps of characteristic energy for precipitating particles over EISCAT, *J. Geophys. Res.*, *106*, 28,925–28,937.

Larsen, M. F. (2002), Winds and shears in the mesosphere and lower thermosphere: Results from four decades of chemical release wind measurements, *J. Geophys. Res.*, *107*(A8), 1215, 10.1029/2001JA000218.

Lewis, R. V., et al. (1994), The electrodynamics of a drifting auroral arc, *Ann. Geophys.*, *12*, 478–480.

Makarevich, R. A., et al. (2006), A first comparison of irregularity and ion drift velocity measurements in the E region, *Ann. Geophys.*, *24*, 2375–2389.

McCormac, F. G., et al. (1987), Circulation of the polar thermosphere during geomagnetically quiet and active times as observed by Dynamics Explorer 2, *J. Geophys. Res.*, *92*, 10,133–10,139.

Millward, G. H., et al. (1996), A coupled thermosphere-ionosphere-plasmasphere model (CTIP), in *Solar Terrestrial Energy Program (STEP) Handbook of Ionospheric Models*, edited by R. W. Schunk, pp. 239–279, Utah State Univ., Logan.

Nozawa, S., and A. Brekke (1995), Studies of the E region neutral wind in the disturbed auroral ionosphere, *J. Goephys. Res.*, *100*, 14,717–14,734.

Opgenoorth, H. J., et al. (1990), Region of strongly enhanced perpendicular electric fields adjacent to auroral arcs, *J. Atmos. Terr. Phys.*, *52*, 449–458.

Price, G. D., and F. Jacka (1991), The influence of geomagnetic activity on the upper mesosphere/lower thermosphere in the auroral zone. Part I: Vertical winds, *J. Atmos. Terr. Phys.*, *53*, 909–922.

Price, G. D., et al. (1995), Simultaneous measurements of large vertical winds in the upper and lower thermosphere, *J. Atmos. Terr. Phys.*, *57*, 631–643.

Rees, D., et al. (1984a), The generation of vertical thermospheric winds and gravity waves at auroral latitudes. Part I: Observations of vertical winds, *Planet. Space Sci.*, *32*, 667–684.

Rees, D., et al. (1984b), The generation of vertical thermospheric winds and gravity waves at auroral latitudes. Part II: Theory and numerical modelling of vertical winds, *Planet. Space Sci.*, *32*, 685–705.

Rees, M. H., and D. Luckey (1974), Auroral electron energy derived from ratio of spectroscopic emissions. Part 1: Model computations, *J. Geophys. Res.*, *79*, 5181–5186.

Ruohoniemi, J. M., and K. B. Baker (1998), Large-scale imaging of high-latitude convection with Super Dual Auroral Radar Network HF radar observations, *J. Geophys. Res.*, *103*, 20,797–20,811.

Schlegel, K. (1988), Auroral zone E-region conductivities during solar minimum derived from EISCAT data, *Ann. Geophys.*, *6*, 129–137.

Schunk, R. W., and J. C. G. Walker (1973), Theoretical ion densities in the lower ionosphere, *Planet. Space Sci.*, *21*, 1875–1896.

Senior, A., et al. (2007), Statistical relationships between cosmic radio noise absorption and ionospheric electrical conductances, *J. Geophys. Res.*, *112*, A11301, doi:10.1029/2007JA012519.

Senior, A., et al. (2008), Comparison of methods to determine auroral ionospheric conductances using ground-based optical and riometer data, *Ann. Geophys.*, *26*, 3831–3840.

Senior, C., et al. (1990), Convection electric fields and electrostatic potential over $61° < \Lambda < 72°$ invariant latitude observed with the European incoherent scatter facility. Part 2: Statistical results, *Ann. Geophys.*, *8*, 257–272.

Störmer, C. (1955), *The Polar Aurora*, pp. 67–80, Oxford Univ. Press, New York.

Thayer, J. P., et al. (1987), Thermospheric neutral wind signatures dependent on the east–west component of the interplanetary magnetic field for Northern and Southern Hemispheres as measured from Dynamics Explorer-2, *Ann. Geophys.*, *5*, 363–368.

Tsunoda, R. T., et al. (1976), The spatial relationship between the evening radar aurora and field-aligned currents, *J. Geophys. Res.*, *81*, 3791–3802.

Vickrey, J. F., et al. (1986), On the current-voltage relationship of the magnetospheric generator at intermediate spatial scales, *Geophys. Res. Lett.*, *13*, 495–498.

Wang, H., et al. (2005), Solar zenith angle and merging electric field control of field-aligned currents: A statistical study of the Southern Hemisphere, *J. Geophys. Res.*, *110*, A03306, doi:10.1029/2004JA010530.

Weimer, D. R. (2001), Maps of ionospheric field-aligned currents as a function of the interplanetary magnetic field derived from Dynamics Explorer 2 data, *J. Geophys. Res.*, *106*, 12,889–12,902.

Wescott, E. M., et al. (2006), The HEX experiment: Determination of the neutral wind field from 120 to 185 km altitude near a stable premidnight auroral arc by triangulating the drift of rocket-deployed chemical trails, *J. Geophys. Res.*, *111*, A09302, doi:10.1029/2005JA011002.

Zmuda, A. J., and J. C. Armstrong (1974), The diurnal flow pattern of field-aligned currents, *J. Geophys. Res.*, *79*, 4611–4619.

C. Anderson, B. A. Carter, and R. A. Makarevich, Department of Physics, La Trobe University, Melbourne, Vic 3086, Australia.

M. Conde, Geophysical Institute, University of Alaska Fairbanks, Fairbanks, AK 99775, USA.

T. Davies and P. L. Dyson, Department of Physics, La Trobe University, Melbourne, Vic 3086, Australia.

R. A. D. Fiori, ISAS, University of Saskatchewan, Saskatoon, SK S7N 5E2, Canada.

M. J. Kosch, Department of Communication Systems, Lancaster University, Lancaster LA1 4WA, UK. (m.kosch@lancaster.ac.uk)